

# Physical Property Characterization of the Waipapa Greywacke: An Important Geothermal Reservoir Basement Rock in New Zealand

Aurelio Melia (✉ [aurelio.melia@libero.it](mailto:aurelio.melia@libero.it))

University of Liverpool (UK) <https://orcid.org/0000-0003-2488-8799>

Daniel Roy Faulkner

University of Liverpool (UK)

David Daniel McNamara

University of Liverpool (UK)

---

## Research

**Keywords:** Geothermal, Greywacke, Permeability, Fracture, Rock Properties, Basement Rock.

**Posted Date:** November 17th, 2021

**DOI:** <https://doi.org/10.21203/rs.3.rs-1071508/v1>

**License:**  This work is licensed under a Creative Commons Attribution 4.0 International License.

[Read Full License](#)

---

# Physical property characterization of the Waipapa Greywacke: an important geothermal reservoir basement rock in New Zealand

Melia, Aurelio<sup>1</sup>, Faulkner, Daniel Roy<sup>1</sup>, McNamara, David Daniel<sup>1</sup>.

<sup>1</sup> Department of Earth, Ocean and Ecological Sciences, University of Liverpool, Liverpool, L69 3GP.

**Keywords:** Geothermal; Greywacke; Permeability; Fracture; Rock Properties; Basement Rock.

Institutional email addresses: faulkner@liverpool.ac.uk ; d.mcnamara@liverpool.ac.uk

Personal email addresses: aurelio.melia@libero.it

Corresponding author: Aurelio Melia

Submission Date: November 12th, 2021.

## ABSTRACT

Greywacke basement rocks in New Zealand host conventional geothermal reservoirs and may supply important hotter and deeper geothermal energy resources in the future. This work combines petrological analyses and physical property measurements of Waipapa greywacke, a basement unit hosting New Zealand geothermal reservoirs, in order to understand better how structurally controlled flow networks develop and channel geothermal fluids within it. Results show intact Waipapa greywacke has high tensile and triaxial compressive strengths, and low intrinsic permeability ( $\sim 10^{-21}$  m<sup>2</sup>). Permeability of intact Waipapa greywacke does not increase significantly during triaxial loading to failure and is accompanied by minimal changes ultrasonic wave velocities. These data taken together suggest that microcrack development during brittle deformation is very limited. Upon failure, the permeability increases by two orders of magnitude and shows similar permeability to tests performed on synthetic, single, mode I fractures in intact Waipapa greywacke. Permeability persists in Waipapa greywacke fractures under confining pressures of at least 150

30 MPa. It is concluded that Waipapa greywacke rocks will not allow fluid flow through the matrix of  
31 the rock and that substantial geothermal fluid flow will only occur through macrofracture networks.

32

33

## 34 **1 INTRODUCTION**

35

36 In New Zealand, both direct use (e.g. heating, bathing, horticulture) and electricity  
37 production from geothermal resources is well developed and continues to expand [Carey et al.,  
38 2015]. Current geothermal development for electricity production in New Zealand utilizes  
39 reservoirs at depths up to ~3.5 km, dubbed the conventional resource. Future development of  
40 geothermal power in New Zealand aims at expanding the use of basement hosted geothermal  
41 resources, including the greywacke basement terranes of the North Island [Mroczek et al., 2016;  
42 Brathwaite et al., 2002; Wood et al., 2001], and newer discoveries proposed in the basement schist  
43 lithologies of the South Island [Sutherland et al., 2017]. Furthermore, future New Zealand  
44 geothermal potential lies in the development of deeper and hotter reservoirs likely hosted within  
45 similar basement lithologies [Bignall, 2011; Sheburn et al., 2003].

46 In basement geothermal reservoirs hosted in greywacke or igneous rocks, fracture and fault  
47 networks control fluid flow [Wood et al., 2001; Sutherland et al., 2017; Wallis et al., 2011; Browne,  
48 1980]. As such, these resources are susceptible to changeable heat fluxes, dynamic fluid flow  
49 regimes, and tectonic stress fields, all of which can exert influence on the physical and mechanical  
50 properties of these fractured reservoir host rocks. Information on the physical and mechanical  
51 properties of basement rocks in New Zealand is thus crucial to their future development as  
52 geothermal resources both at conventional development depths and at novel, deeper depths.  
53 Furthermore, such dynamic environments generate fluid-rock interactions, which can alter the  
54 mineralogy and texture of reservoir host rocks, in turn modifying the physical properties, which

55 govern their mechanical behaviour and subsequent structural network development [Siratovich et  
56 al., 2015]. In order to optimize and maintain structurally hosted geothermal resources, studies of  
57 their physical properties, their interactions, and their dynamic evolution due to fluid interactions  
58 need to be studied to understand the effects they produce in the subsurface reservoir [Gupta and  
59 Sukanta, 2006; Di Pippo, 2008; Grant and Bixley, 2011].

60 To date, few data on the thermo-physical properties of New Zealand greywacke basement  
61 rocks exist [Mielke et al., 2016, McNamara et al., 2014; Richards and Read, 2007]. This study aims  
62 to enhance the understanding of the physical properties of these important geothermal reservoir  
63 rocks by presenting new data on the physical, mechanical, and elastic properties on the Waipapa  
64 greywacke terrane. This basement terrane is known to host geothermal reservoirs in the Ngawha  
65 Geothermal Field in Northland, and has the potential to host deeper geothermal resources in the  
66 Taupo Volcanic Zone (TVZ). Rock texture and microstructure analysis, combined with physical  
67 property determination (uniaxial compressive strength (UCS), tensile strength, triaxial compressive  
68 strength, static and dynamic elastic properties, porosity, density, seismic wave velocity, and  
69 permeability) of Waipapa Terrane greywacke samples presented here provide new information on  
70 the physical properties controlling brittle deformation in this lithology, the process necessary for it  
71 to act as a geothermal reservoir. Data presented here will contribute towards the improved  
72 construction of thermo-hydro-mechanical-chemical models of this basement terrane to assist in de-  
73 risking of future New Zealand geothermal systems and other similarly hosted geothermal reservoirs  
74 globally.

75

## 76 **1.1 Geological Setting**

77 The Waipapa Terrane in New Zealand spans a significant portion of the northwest half of  
78 New Zealand's North Island, outcropping from the northwest border of the TVZ, and northwards  
79 into Northland (Figure 1). Permian to Jurassic units comprise the terrane in a complex sequence of  
80 indurated and metamorphosed volcanoclastic sandstones and siltstones [Adams et al., 2009;

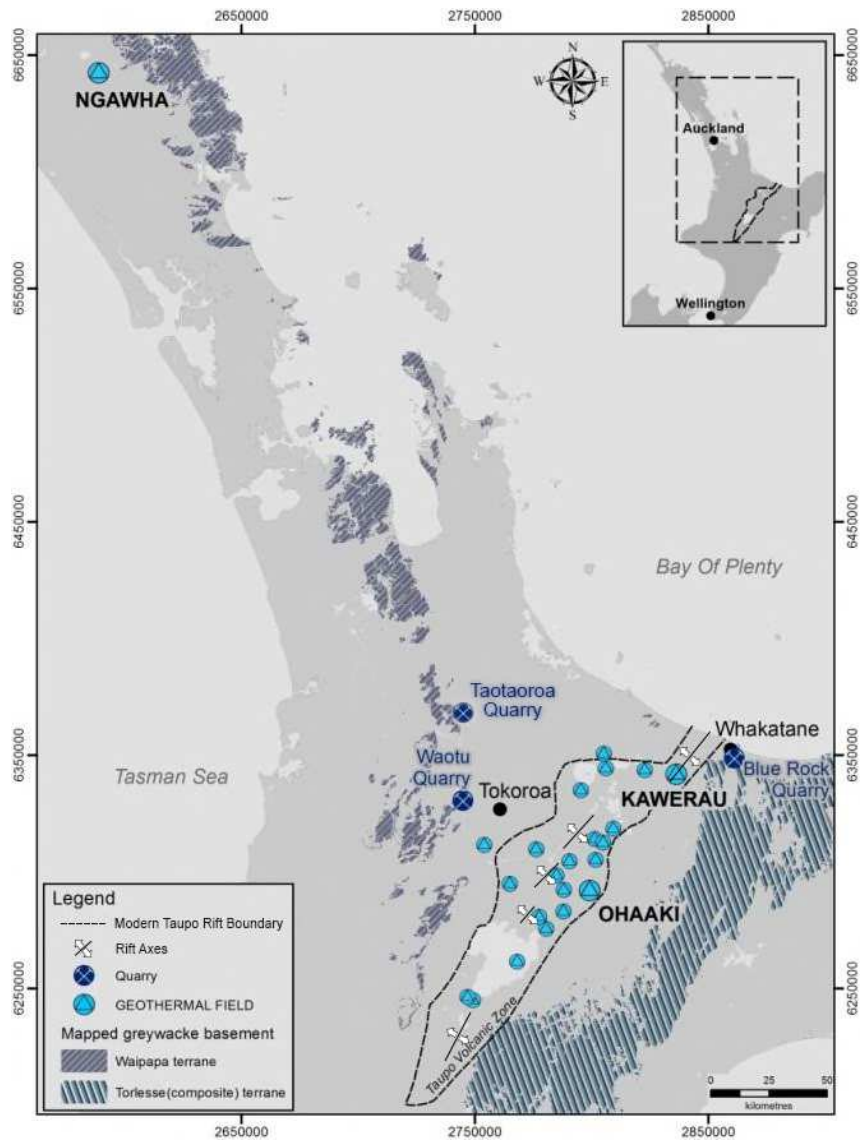
81 Beetham and Watters, 1985]. Following Begg & Mazengarb (1996), in New Zealand the greywacke  
82 sequences are generally identified as medium to dark grey, coarse to medium grained, lightly  
83 metamorphosed sandstones. Grains are poorly sorted and consist of angular quartz and feldspar, and  
84 lithic fragments of metamorphic and igneous rocks. The intergranular material consists of clay  
85 minerals formed during induration or low-grade metamorphism. Greywacke sandstones may be  
86 interbedded with lightly metamorphosed mudstones (argillite), usually layers of clay, silt, or mud,  
87 generally dark to black in colour, yet occasionally red when there is a high content of iron bearing  
88 minerals. The proportions between mudstone and sandstone are spatially variable within the  
89 Waipapa Terrane. Geothermal expression in this unit is well documented at the Ngawha  
90 Geothermal Field in Northland, and potentially within the buried basement units underneath the  
91 modern (>2 Ma) volcanoclastic deposits of the TVZ.

92         Locally, at the Ngawha Geothermal Field, Waipapa Terrane basement hosting the  
93 geothermal resource is composed of grey-green argillites and massive, quartzo-feldspathic  
94 greywacke sandstones which have experienced low-grade metamorphism (prehnite-pumpellyite  
95 grade [Mayer, 1968]), and are strongly hydrothermally altered and veined with common fault  
96 breccia textures [Bayrante and Spörli, 1989; Cox and Browne, 1998; Sheppard, 1986]. Waipapa  
97 greywacke basement is not yet drilled within the TVZ, an extensional intra-arc basin formed as a  
98 consequence of oblique subduction of the Pacific Plate underneath the North Island of New Zealand  
99 [Sheppard, 1986; Wilson et al., 1995]. Torlesse Terrane greywacke basement rock has been  
100 penetrated by drilling in the Kawerau, Ngatamariki, Ohaaki, Rotokawa, and Tauhara geothermal  
101 fields [Wood et al., 2001; Adams et al., 2009; Cole and Spinks, 2009; Cant et al., 2018; McNamara  
102 and Massiot, 2016; McNamara et al., 2016, Bignall et al., 2010], and at Kawerau Geothermal Field  
103 hosts geothermal resources. The suture between the Waipapa and Torlesse terranes is thought to  
104 occur somewhere within the TVZ underneath the infill units but a precise location and depth is  
105 undetermined [Adams et al., 2009; Milicich et al., 2013a]. However, given that seismic evidence  
106 points to brittle deformation reaching potential depths of ~6 to 8 km [Bibby et al., 1995], Waipapa

107 terrane greywacke holds significant potential as a reservoir for hotter and deeper geothermal  
108 resources within the TVZ [Bignall, 2011].

109 Limited data exist on the thermo-physical properties of the Waipapa terrane greywacke  
110 lithologies. A 3.7% porosity measurement, which included a structural component, was measured  
111 by McGuinness [McGuinness, 1984]. UCS values of Waipapa terrane greywacke of ~193 MPa are  
112 recorded by Richards and Read (2007). McNamara et al. (2014) describe densities of ~2.71 g/cm<sup>3</sup>,  
113 tensile strength ranges of 20-36 MPa, UCS values of 300-310 MPa, static Poisson's ratio and  
114 Young's moduli of 0.28 and 70 GPa respectively, cohesion values of 51 MPa, a 0.93 coefficient of  
115 internal friction ( $\mu$ ), nuclear magnetic resonance porosities of 2%, and P-wave velocities ( $V_p$ ) ranges  
116 of 6 - 6.25 km/s. Mielke et al. (2016) document similar values for the properties noted in  
117 McNamara et al. (2014) with the only exceptions being lower  $V_p$  values (~5.6 km/s), lower UCS  
118 values (123-245 MPa), and lower Young's Modulus (~20-27 GPa). Porosity values of ~1%,  
119 permeability of  $<1 \times 10^{-16}$ , thermal conductivity (~2.5 Wm<sup>-1</sup>K<sup>-1</sup>) and diffusivity (~1.14-1.24 x 10<sup>-6</sup>  
120 m<sup>2</sup>/s), specific heat capacity of ~0.74-0.87 kg.m<sup>2</sup>/K.s<sup>2</sup>, and a shear-wave velocity ( $V_s$ ) of 3 km/s are  
121 also recorded.

122



123

124 **Figure 1:** Map of the North Island of New Zealand showing outcropping basement terrane rocks, major structural  
 125 components of the TVZ, geothermal field locations, and the locations of the quarries used for sampling for this work.  
 126 Modified from McNamara et al. (2014).

127

128

## 129 **2 METHODS AND MATERIALS**

### 130 **2.1 Materials and Sample Preparation**

131 Samples of Waipapa greywacke terrane were acquired from quarry outcrops in order to test  
 132 their physical and mechanical properties. Waipapa samples are sourced from Taotaoroa Quarry  
 133 (TTGW), which is located between Cambridge and Matamata, ~8 km north of Karapiro Lake.  
 134 While outcrops where samples are acquired show the Waipapa greywacke to be layered and

135 fractured, the samples tested here contain no discernible anisotropy with respect to internal fabrics.  
136 All the rock deformation data presented in this work were collected at the Rock Deformation  
137 Laboratory at the University of Liverpool, and SEM images were collected using a JEOL JSM  
138 7001F FEG-SEM in the SEM Shared Research Facility, Albert Crewe Centre for Electron  
139 Microscopy at the University of Liverpool. Twenty-five, 20 mm diameter x 50 mm height  
140 specimens were cored and squared from samples of Waipapa greywacke sandstones from Taotaoroa  
141 Quarry. Squareness of the cored samples was better than 0.01 mm or less [Paterson and Wong,  
142 2015]. A selection of these specimens was used to make ten, 20 mm diameter x 10 mm height disks  
143 utilized for tensile strength measurements, and two cores (of the same size) for permeability  
144 measurements where a macroscopic mode I fracture was induced in the samples. Three thin sections  
145 of Waipapa greywacke from Taotaoroa Quarry were made for petrological observations using an  
146 optical microscope. Finally, the sample taken to failure during triaxial testing was impregnated with  
147 epoxy resin and cut parallel to the core axis and perpendicular to the shear fracture plane, polished  
148 and utilized for imaging of the deformed specimen in an XL30 Philips scanning electron  
149 microscope (SEM).

150

## 151 **2.2 Porosity measurements and bulk density**

152 Porosity estimates are determined from cores using a helium multipycnometer model (MVP-  
153 D160-E, Quantachrome Instruments). The porosity was calculated for seventeen samples of  
154 Waipapa greywacke. Bulk density was calculated for three Waipapa greywacke cores, using their  
155 mass and solid volume.

156

## 157 **2.3 Tensile strength**

158 Brazilian tests, conforming to ATSM standards (ATSM D3967-08), were performed on 20  
159 mm diameter disks of greywacke basement rock, with a thickness-to-diameter ratio ( $t/D$ ) between  
160 0.2 and 0.75. Tensile strength is calculated with the following equation:



161

$$\sigma_t = \frac{2P}{\pi LD} \quad (1)$$

163

164 where:  $\sigma_t$  is the splitting tensile strength (MPa), P is the maximum force applied indicated by  
165 the machine (N), L is the thickness of the specimen (mm), D is the diameter of the specimen (mm).

166

167

168

## 169 **2.4 Uniaxial compressive strength**

170 UCS experiments were carried out on ten samples from Taotaoroa Quarry. Axial and  
171 circumferential strain gauges were attached to the samples during testing. Samples were then  
172 brought to failure using a uniaxial press. Static Young's modulus ( $E$ ) and static Poisson's ratio ( $\nu$ )  
173 are estimated from the gradient of a linear elastic region of the UCS test results (from 40-120 MPa).

174

## 175 **2.5 Triaxial loading test**

176 A single triaxial compressive test ( $\sigma_1 > \sigma_2 = \sigma_3$ ) was carried out on a greywacke core in  
177 order to obtain the lithology's strength under confining pressure conditions of 20 MPa and a pore  
178 pressure of 5MPa ( $\bar{\sigma} = 15$  MPa) to enhance our understanding of how this lithology undergoes  
179 shear fracture at ~1 km depth, and to ensure repeatability of results delivered in McNamara et al.  
180 (2014). Furthermore, the evolution of permeability and P and S wave velocity were monitored to  
181 establish the development of these properties during loading to failure. We used a triaxial  
182 deformation rig able to perform triaxial experiments up to 250 MPa confining pressure (servo  
183 controlled), 250 MPa pore pressure (servo controlled), and ~1000 MPa differential stress with a  
184 load capacity of 300 kN [Faulkner and Armitage, 2013] (Figure 2). Figure 2 shows the layout of  
185 this apparatus, illustrating where the sample is situated within the pressure vessel. It also shows the

186 internal force gauge that provided high resolution measurements of the axial force that was applied  
187 to the sample via a screw-driven actuator below the vessel illustrated in Figure 2.

188  $V_p$  and  $V_s$ , and permeability measurements of the sample are measured axially during this  
189 experiment. The position of the piezoelectric crystals (lead-zircon titanate) within the assembly are  
190 illustrated in Figure 2. Axial loading proceeded at a displacement rate of 0.1 microns/s and paused  
191 at various intervals in order to obtain  $P$ - and  $S$ - wave velocity and permeability measurements  
192 (detailed in Section 2.7). The axial displacement reported is corrected for the elastic distortion of  
193 the loading column, which is 180 kN/mm for the apparatus.

194

195

## 196 **2.6 Elastic wave velocities and dynamic elastic moduli**

197 Ultrasonic wave velocities ( $P$ - and  $S$ - wave) were measured along sample axes while loaded  
198 to failure in both uniaxial compression and triaxial testing. These tests were carried out in order to  
199 understand how the wave velocities develop as microcrack networks develop under increasing  
200 stress, providing insight into the change in microcrack density in the samples during deformation  
201 (e.g. Schubnel et al., 2003). Values are determined under varying levels of axial stress during UCS  
202 testing, and under various levels of axial stress with constant confining pressures during triaxial  
203 testing. Physical property characterizations are summarized in Table 2.

204 Velocity data were used to calculate a dynamic Young's modulus ( $E_d$ ) and dynamic  
205 Poisson's ratio ( $\nu_d$ ) for these samples, using the below equations and assuming isotropy [Kuttruff,  
206 1991]:

207

$$208 \quad E_d = \frac{\rho V_s^2 (3V_p^2 - 4V_s^2)}{V_p^2 - V_s^2} \quad (2)$$

209

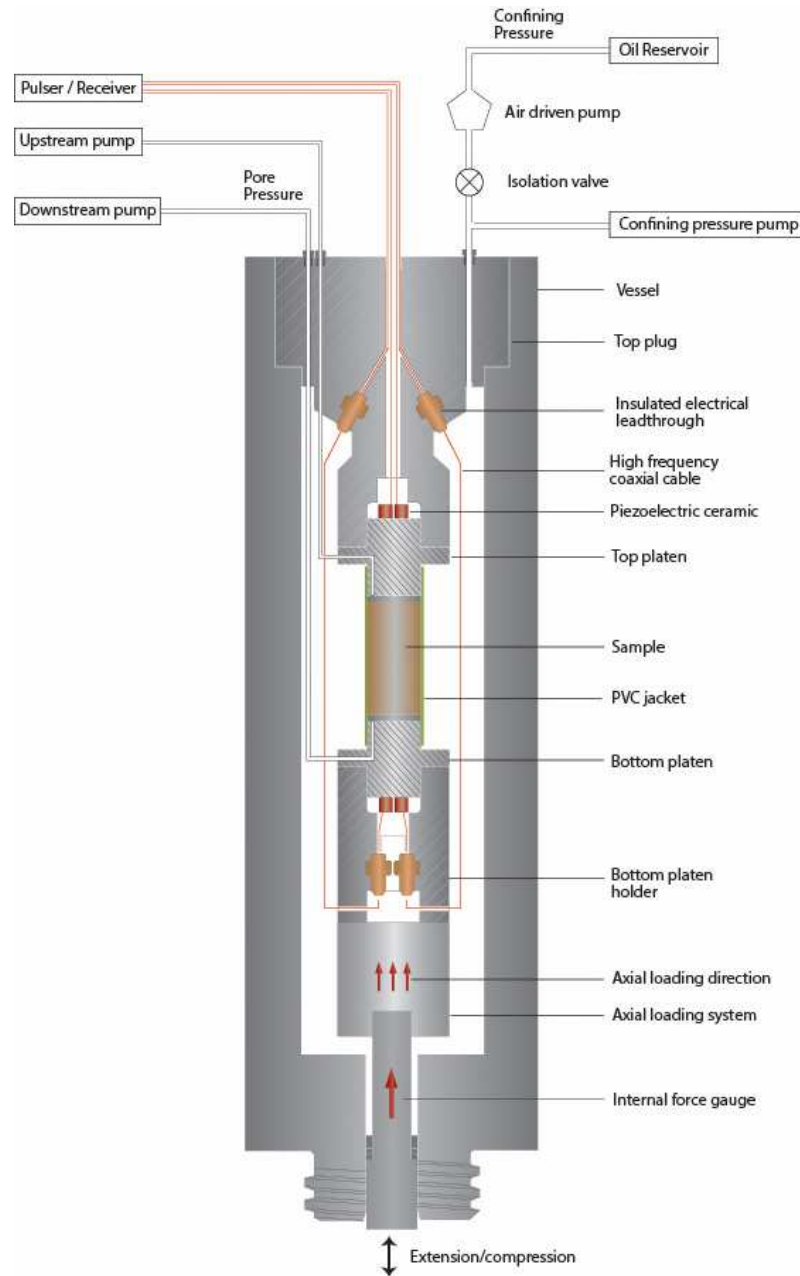
$$210 \quad \nu_d = \frac{V_p^2 - 2V_s^2}{2(V_p^2 - V_s^2)} \quad (3)$$

211

212 where  $\rho$  is the density ( $\text{g/cm}^3$ ). The change in the sample's density, calculated from the variation in

213 volumetric change which occurs during uniaxial compression, was accounted for in the analysis.

214



215

216 **Figure 2:** A schematic illustration of the sample assembly contained within the pressure vessel used for the  
217 experiments described. It also highlights the position of the piezoelectric crystals within the assembly that  
218 are used for the  $P$  and  $S$  wave velocity measurements [Faulkner and Armitage, 2013].

219

220

221

## 222 **2.7 Permeability measurements**

223 To examine fluid flow properties of the Waipapa Terrane greywacke, permeability tests  
224 were carried out on both intact samples and samples containing a synthetic single fracture.  
225 Permeability measurements were performed using the pulse-transient method [Brace et al., 1968]  
226 with deionised water used as the pore fluid. When the measurement begins, the upstream and  
227 downstream reservoir pressures of the sample are equilibrated and equal. A small increase (<1  
228 MPa) of the upstream reservoir pressure or a decrease of the downstream reservoir pressure is then  
229 imposed to apply a pressure gradient across the sample. The decay characteristics of this pressure  
230 pulse, monitored in the upstream or downstream reservoir or both, may then be used to obtain a  
231 value for permeability.

232 As previously mentioned, permeability measurements were made during the triaxial  
233 compression tests to monitor permeability evolution as intact greywacke approaches failure.  
234 Permeability measurements were made for each pressure step (every 20 kN, or 63.91 MPa increase  
235 in load). The first permeability measurement was taken at 0 MPa (no load applied), with subsequent  
236 measurements made at compressive stresses of 20 (63.91 MPa), 40 (127.81 MPa), 60 (191.72  
237 MPa), 80 (255.62 MPa), 90 (287.57 MPa), 95 (303.55 MPa) and finally 100 kN (319.52 MPa)  
238 where brittle failure occurred.

239 In order to understand how the permeability of single fracture responds to varying stress  
240 conditions, two intact greywacke rock cores (20 mm diameter x 10 mm height) were placed in a  
241 Brazilian loading jig, then loaded to failure in order to produce a single fracture plane [Nara et al.,  
242 2011]. These samples were then carefully placed in a polyurethane jacket and put into a triaxial  
243 testing apparatus to hydrostatically load the specimen and measure evolving fracture permeability.  
244 For both specimens, permeability was recorded initially at 40 MPa confining pressure, with  
245 subsequent measurements taken every 5 MPa up to 110 MPa. After that, permeability  
246 measurements were taken at 120, 130 and 150 MPa. The procedure used here follows that of Nara  
247 et al. [Nara et al., 2011].

248 **Table 1:** List of samples examined in this study and the experimental tests performed on each. TTGW = Taotaoroa  
 249 quarry greywacke; SF = Single Fracture experiment. Numbers in brackets (e.g. (x3)) indicate the number of times that  
 250 test was carried out on that sample. Samples TTGW\_11\_3\_H1160 and TTGW\_11\_3\_H1161 are thin sections.  
 251

Sample	Uniaxial	Triaxial	Brazilian	Vp - Vs	Porosity	Permeability	SEM	XPL	S.F.	Density
TTGW_11_3_H1160								✓		
TTGW_11_3_H1161								✓		
TTGW_11_3_4_triax		✓		✓	✓	✓	✓	✓		
TTGW_11_2_1	✓									
TTGW_11_2_2	✓									
TTGW_11_2_3	✓									
TTGW_11_2_4	✓									
TTGW_11_3_1					✓					
TTGW_11_3_2					✓					
TTGW_11_3_3					✓					
TTGW_11_3_5					✓	✓ (x18)			✓	
TTGW_11_3_6	✓				✓					
TTGW_11_3_7					✓					
TTGW_11_3_8			✓ (x3)		✓					
TTGW_11_3_10				✓	✓					
TTGW_11_3_11	✓									✓
TTGW_11_3_12	✓			✓						✓
TTGW_11_3_13	✓			✓						✓
TTGW_11_3_14	✓			✓						
TTGW_11_3_16					✓					
TTGW_11_3_17					✓	✓ (x18)	✓		✓	
TTGW_11_3_18			✓ (x3)		✓					
TTGW_11_3_19					✓					
TTGW_11_3_20			✓		✓					
TTGW_11_3_21			✓		✓					
TTGW_11_3_22					✓					
TTGW_11_3_23			✓ (x2)		✓					

252

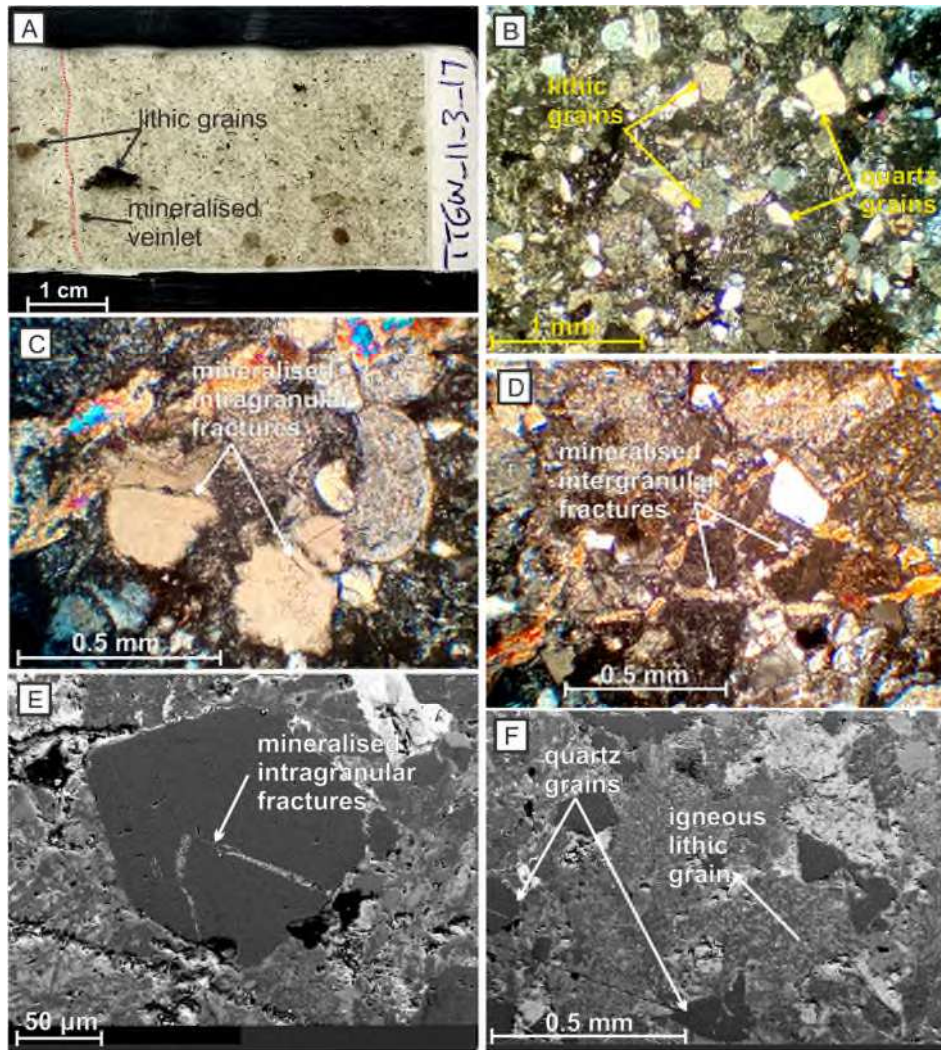
253

## 254 **3 RESULTS**

### 255 **3.1 Petrology**

256 From examination, Waipapa Terrane samples used in this study are composed of a medium  
257 to coarse grained (0.25–1.5 mm), greywacke sandstone consisting of abundant to common,  
258 subangular–subrounded, detrital quartz, plagioclase, and abundant lithic fragments ( $\leq 5$  mm sizes)  
259 (Figure 3). Lithic fragments are made of andesitic, basaltic, and rhyolitic lavas with granophyric  
260 textures, and siltstone. Some lava lithics show a trachytic texture. The greywacke sandstone is clast  
261 supported and matrix poor. Matrix is composed of indurated clay/silt. Chlorite, calcite, quartz, and  
262 occasional epidote are found as vein minerals. In general, the Waipapa samples are moderately  
263 altered to chlorite, leucoxene and clay with some weak epidote alteration. Plagioclase crystals in  
264 places are weakly altered to clays while detrital biotite crystals are relatively fresh. Within the rock  
265 andesite lithic fragments show some albitization. The groundmass is altered to chlorite and detrital  
266 plagioclase is partially altered to clay. Mineralization within observed microfractures in these  
267 samples indicates that these crack networks at one point operated as fluid flow pathways.

268



269  
 270 **Figure 3:** A) Photograph of thin section of sample TTGW\_11\_3\_17 showing grain size variation and  
 271 mineralised veinlets (red line), B) Photomicrograph (XP; TTGW\_11\_3\_17) showing typical grain size and texture  
 272 of Waipapa basement greywacke C) Photomicrograph (XP; TTGW\_11\_3\_17) showing mineralised  
 273 intragranular fractures in quartz grains, D) Photomicrograph (XP; TTGW\_11\_3\_17) showing mineralised  
 274 intergranular veinlets in Waipapa greywacke, E) SEM backscatter image (TTGW\_11\_3\_17) showing  
 275 mineralised intragranular fractures within a quartz grain, F) SEM backscatter image (TTGW\_11\_3\_17) showing  
 276 typical grain sizes and textures of Waipapa greywacke basement and the igneous textures noted in lithic grains. Qz = quartz, Pl  
 277 = plagioclase.

278

### 279 3.2 Porosity and bulk density

280 Table 2 provides an overview of the mechanical (tensile and unconfined strength), elastic,  
 281 and physical properties of intact Waipapa greywacke.

Property	Measured Range	# of Tests	Mean	Standard Deviation
Tensile Strength	14.4 - 32.42	10	21.07	8.28

(MPa)				
UCS (MPa)	205 - 384	10	285.6	60.17
Poisson's Ratio ( $\nu_S$ )	0.19 - 0.36	10	0.316	0.1
Young's Modulus ( $E_S$ ) (GPa)	54 - 85	10	72.8	9.04
Poisson's Ratio ( $\nu_D$ )	0.28 - 0.30	3	0.29	0.01
Young's Modulus ( $E_D$ ) (GPa)	80 - 84	3	81.7	2.08
Density ( $\rho$ ) (g/cm <sup>3</sup> )	2.721 - 2.731	3	2.726	0.0051
Porosity ( $\phi$ ) (vol%)	0.841 - 1.304	17	1.035	0.152

282

283

**Table 2:** Summary of the measured physical properties of Waipapa greywacke from this study.

284

### 285 3.3 Tensile strength

286

287

288

289

290

291

### 292 3.4 Uniaxial compressive strength (UCS) and static elastic moduli

293

294

295

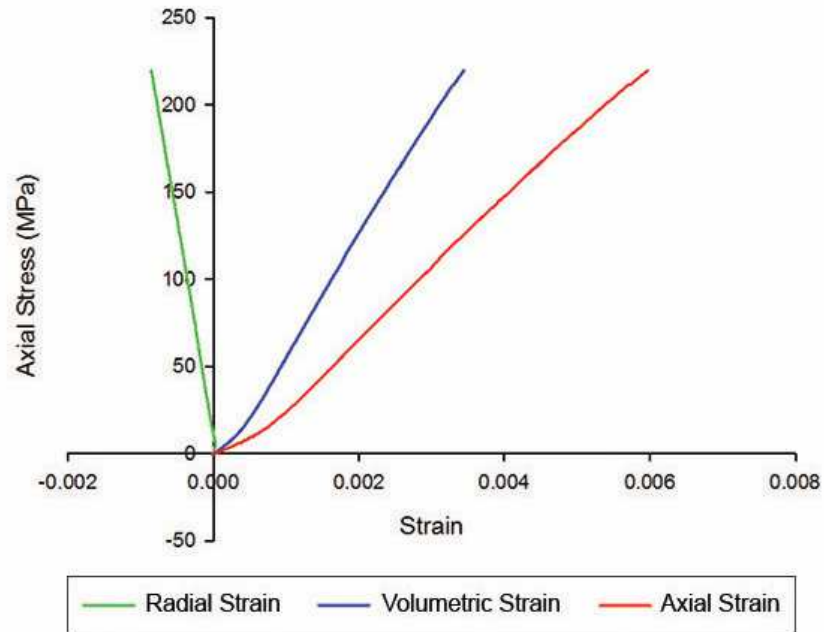
296

297

A standard deviation in tensile strength for the Waipapa greywacke samples indicates some variability (Table 2). Studies about the precision and reproducibility of tensile strength tests have been made by ASTM testing multiple specimens of different rocks (ASTM, D3967 - 08). Variability of tensile strengths measured here is not outside the norm for these types of experiments [Gale and Holder, 2008].

For all UCS tests (Table 1), stress-strain curves show a slight concave-upwards trend at low loads, followed by a linear region showing no ductile behavior up to failure (Figure 4). No discernible yield point was observed before failure. Static Young's moduli range between 54 and 85 GPa and static Poisson's ratios range from 0.19 to 0.36 (Table 2).





298

299 **Figure 4:** Stress-strain curves obtained from the uniaxial test of the Waipapa greywacke sample  
 300 TTGW\_11\_2\_2. These results are typical of the UCS tests in general.

301

302

### 303 3.5 Triaxial compressive strength

304 Permeability measurements (Table 1) performed prior to the start of the triaxial test provide  
 305 an intact rock permeability of  $1.65 \times 10^{-21} \text{ m}^2$ . Axial loading proceeded at a displacement rate of 0.1  
 306 microns/s, and the loading was stopped at regular intervals in order to obtain P and S wave velocity  
 307 and permeability measurements (Figure 9). The axial displacement reported is corrected for the  
 308 elastic distortion of the loading column which is 180 kN/mm for the apparatus.

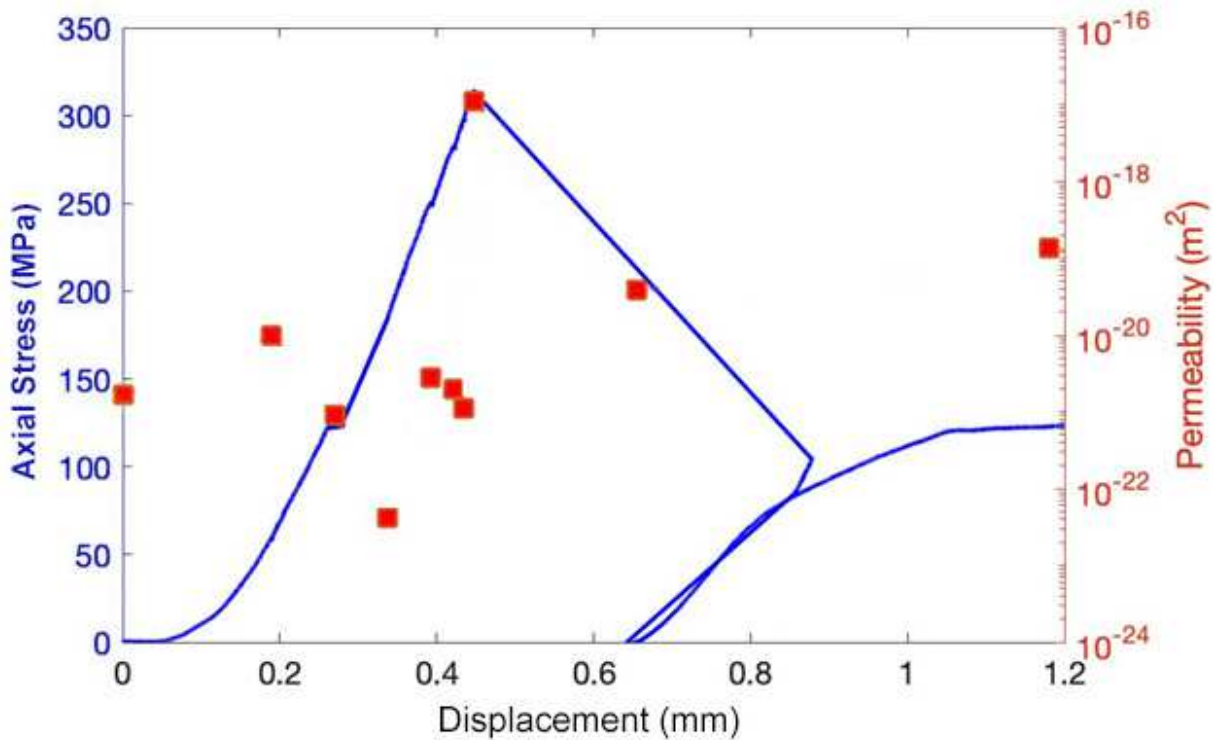
309 The loading curve in Figure 5 shows a typical, initial concave upwards trend, then quasi-  
 310 linear loading, the slope of which provides a static Young's modulus of ~55 GPa. No yield is  
 311 observed as failure (314 MPa) is approached, and the sample fails while still under quasi-linear  
 312 loading. Reloading of the sample after failure occurs along a shallower gradient indicating the  
 313 fractured sample is more compliant, and a residual strength of ~120 MPa is recorded.

314

315 Throughout the triaxial test, as strain accumulates before failure is reached (Figure 5), the  
316 permeability does not vary greatly. The small changes observed up to displacements of  $\sim 0.42$  mm  
317 are likely a result of measurement variability. Only immediately before failure is a dramatic  
318 increase in permeability seen, where the permeability increases by  $\sim 4$  orders of magnitude. During  
319 this part of the loading history, the pore volume shows a decrease of  $2.73 \text{ mm}^3$  (Figure 6). Most of  
320 this decrease occurred during the initial loading of the sample.

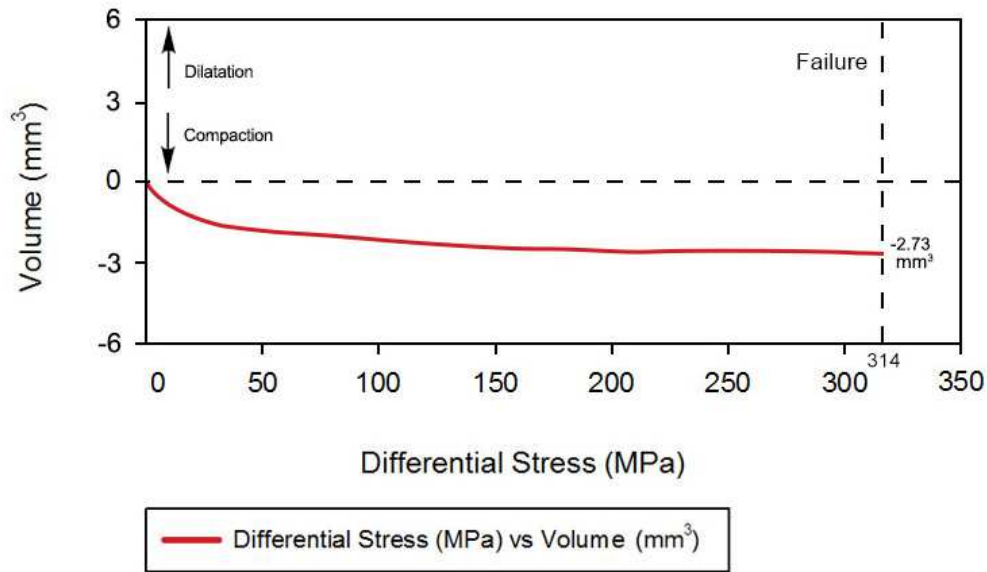
321 Following failure and unloading of the sample, the permeability is much lower than seen at  
322 peak stress. Following residual strength yield, and a small amount of shearing along the shear  
323 fracture created during loading, the permeability increases slightly again.

324  
325  
326



327  
328 **Figure 5:** Results from the triaxial loading experiment. The blue line shows loading of the sample to failure,  
329 followed by unloading and reloading the sample with the shear fracture to residual failure. The red squares  
330 show the evolution of permeability during the loading history.

331  
332



333

334

**Figure 6:** Pore volume change with increasing differential stress during the triaxial test.

335

336

### 337 3.6 Scanning electron microscopy observations

338

339

340

341

342

343

344

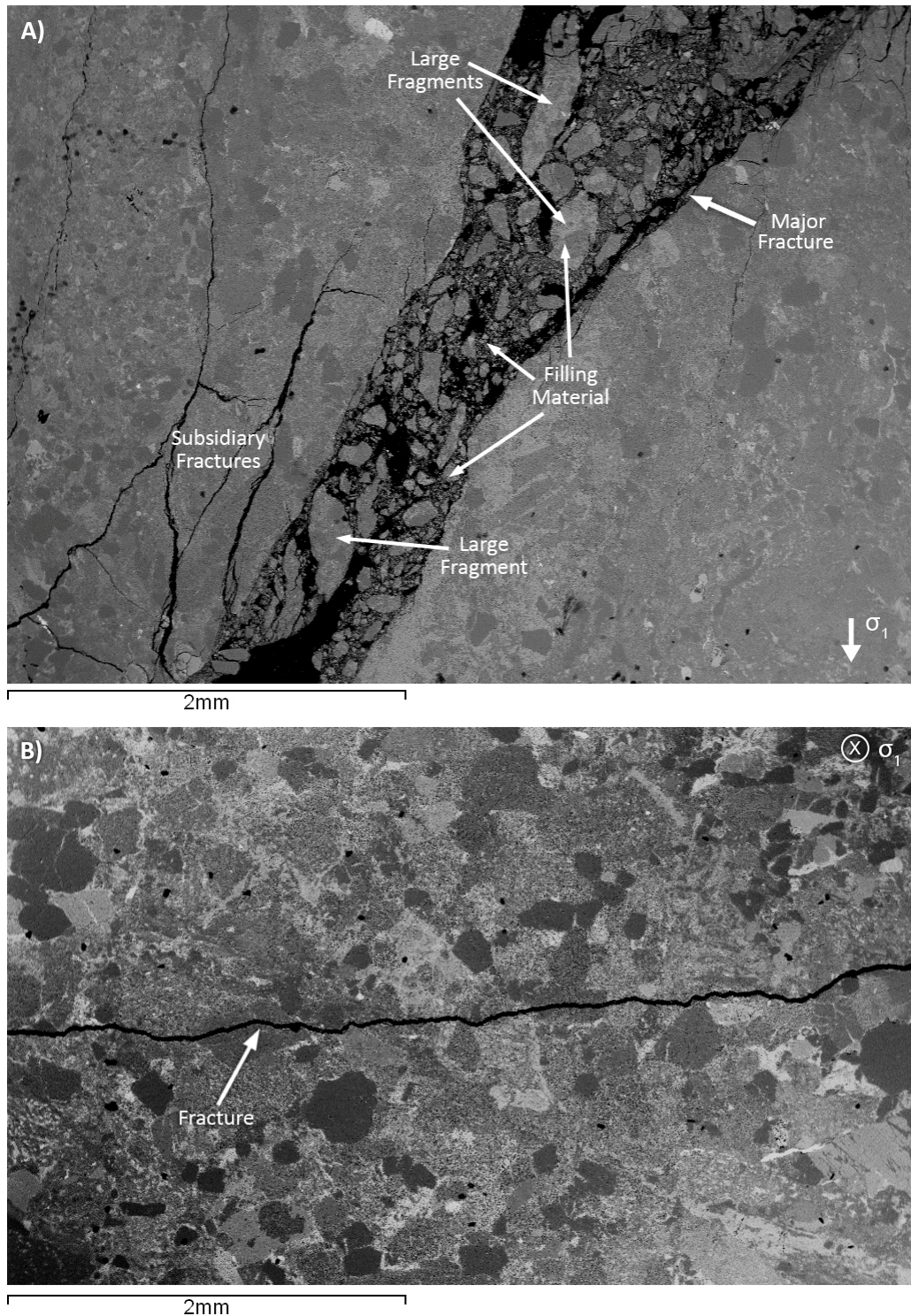
345

346

347

348

SEM observations (Table 1) of the shear fracture generated by the failure of the core during the triaxial test reveal it is filled with fragments of greywacke material (Figure 7a). The upper extremity of the fracture, where the sample comes into contact with the loading platen, widens and has a triangular shape, filled with large greywacke fragments ( $\leq 0.675$  mm) set in a finer matrix ( $\leq 200$   $\mu\text{m}$  sized cement grain). The typical aperture of the fracture is  $<1$  mm. A network of subsidiary fractures develops close to both sides of the main rupture. This subsidiary fracture network is variable and includes both relatively wide fractures and clusters of narrower cracks. The subsidiary fractures have variable morphologies that are broadly parallel and sub-parallel to the main fracture, and parallel to the loading direction. Very few subsidiary brittle deformation features are observed at greater distance from the main rupture in the tested sample.



349  
 350 **Figure 7:** A) SEM image of the greywacke sample TTGW\_11\_3 brought to failure in triaxial conditions. The deformed  
 351 sample was mounted in epoxy resin and cut and polished for imaging within the SEM. This image displays the shear  
 352 fracture and its filling material. A microfracture network is visible to the left side of the primary shear fracture. B) This  
 353 image is the result of an assembly of images that have been acquired using the SEM. It shows an induced fracture in a  
 354 greywacke disk (TTGW\_11\_3\_17) using the Brazilian jig.

355

356 The synthetically produced fractures from Brazilian loading (Figure 7b) show very little  
357 comminution and, in contrast to the shear fracture (Figure 7a), few fragments contained within the  
358 fracture. Fracture walls are a mixture of tortuous and straight, and rough and smooth, and the  
359 fracture width is consistent (~25  $\mu\text{m}$ ). There is no development of a damage zone or subsidiary  
360 fractures around the main fracture (Figure 7b). Similar post-failure conditions occurred for  
361 TTGW\_11\_3\_5 sample (Figure 10).

362

363

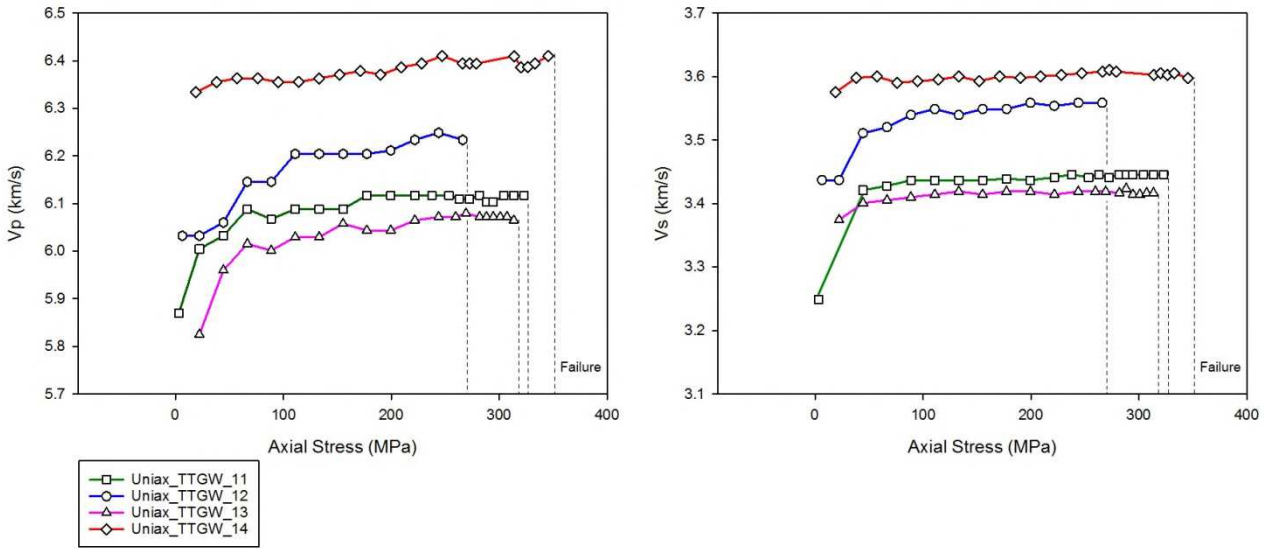
### 364 3.7 $V_p$ , $V_s$ , and dynamic elastic moduli

365  $V_p$  and  $V_s$  values were acquired during both uniaxial and triaxial tests (Table 1). The  $P$ -wave  
366 and  $S$ -wave data were measured along the sample axis. From uniaxial tests,  $V_p$  varies from 6,072 to  
367 6,410 m/s (Figure 8), and  $V_s$  varies from 3,423 to 3,605 m/s. From the triaxial test, peak  $V_p$  is 6,334  
368 m/s and peak  $V_s$  is 3,647 m/s. Dynamic Poisson's ratio was in the range of 0.28 - 0.30 and dynamic  
369 Young's modulus was in the range 80 to 84 GPa.

370 Figure 8 shows the trend of  $V_p$  and  $V_s$  for Waipapa greywacke during uniaxial testing. Data  
371 shows an initial rapid increase in  $V_p$  and  $V_s$  as the differential stress is increased (Figure 8). After  
372 that,  $V_p$  and  $V_s$  assume a sub-horizontal trend and show little changes up to the point of failure. In  
373 detail, all the  $V_p$  curves show fluctuation with a general increasing trend, while, for the  $V_s$ , in the  
374 beginning the trend is upward, then it levels out until failure. Data from the triaxial test reveals a  
375 similar trend between  $V_p$ ,  $V_s$ , and axial stress (Figure 9).

376

377



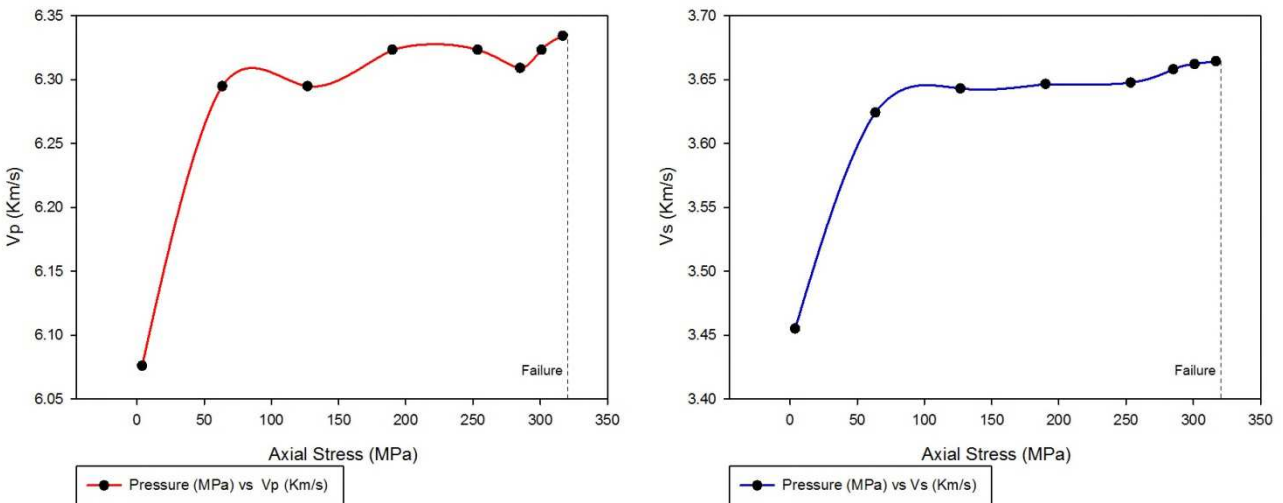
378

379

380

381

**Figure 8:** Seismic wave velocities ( $V_p$  and  $V_s$ ) measured along the sample axis during uniaxial compressive tests.



382

383

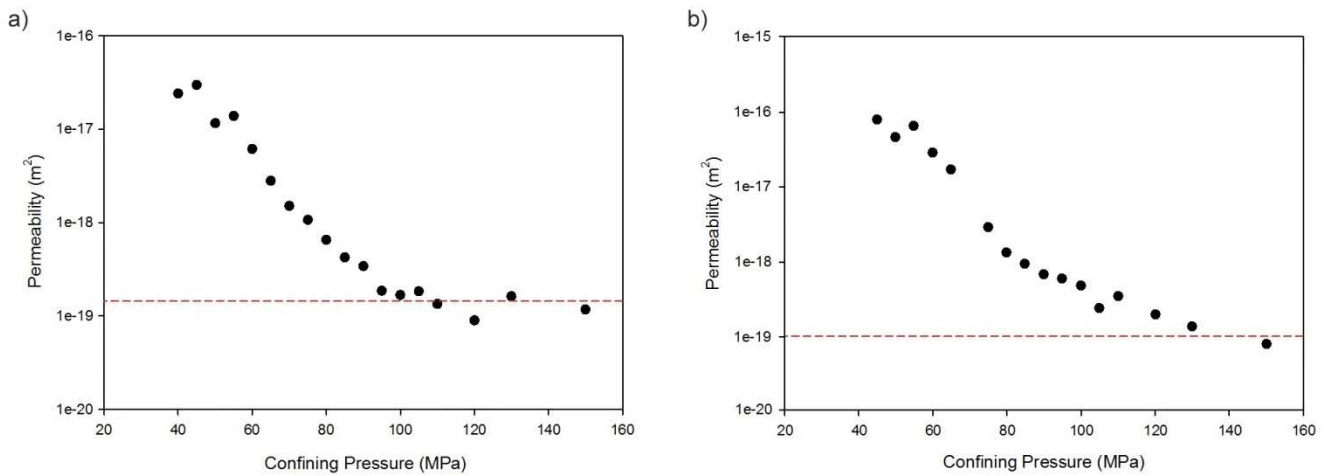
**Figure 9:** Seismic wave velocities ( $V_p$  and  $V_s$ ) measured during triaxial compressive test.

384

### 385 3.8 Single fracture permeability

386 As confining pressure increased a monotonic decrease in permeability is observed for the  
 387 single, Mode I fracture in Waipapa greywacke (Figure 10). In both experiments, a similar trend in  
 388 permeability response is observed, with permeability measurements (Table 1) between  $10^{-16} \text{ m}^2$  and  
 389  $10^{-17} \text{ m}^2$  made at 40 MPa confining pressure, and permeability measurements of  $\sim 10^{-19} \text{ m}^2$  made at  
 390 150 MPa confining pressures. At no point in the experiments did the fracture cease to allow the

391 transmission of fluid along it. We saw that even with 150 MPa confining pressure the permeability  
392 was still higher than measured for the intact samples (Figure 10).



393  
394 **Figure 10:** Graph of permeability against confining pressure through a single fracture (samples TTGW\_11\_3\_5 (a) and  
395 TTGW\_11\_3\_17 (b)). Red dashed line indicates where permeability becomes stable.

396

397

## 398 4 DISCUSSION

399 The physical properties of a lithology affect its ability to transmit fluid within it. The matrix  
400 permeability of a rock is the key factor influencing fluid flow in a rock type, which in turn is  
401 strongly influenced by porosity, pore connectivity and, for low porosity lithologies, microfractures.  
402 Beyond matrix permeability a lithology's ability to transmit fluid is dictated by the presence of  
403 structures [Evans et al., 2005], and the formation of structural permeability within a lithology is  
404 related to the mechanical properties of the rocks that constitute it. We discuss here our findings in  
405 the context of how they help understand fluid flow within Waipapa greywacke basement units.

406

### 407 4.1 The role of microfractures in Waipapa greywacke mechanical strength

408 The Waipapa greywacke mechanical strength reported here is high. As a comparison, the  
409 mechanical strength of the Waipapa greywackes (Table 3) is higher than that found in other

410 lithologies reported as mechanically strong such as Westerly granite (UCS strength ~200 MPa  
411 [Mitchell and Faulkner, 2008; Heap and Faulkner, 2008]), or the Rotokawa Andesite, another  
412 important geothermal reservoir rock in the TVZ (UCS strength of 60-211 MPa; [Siratovich et al.,  
413 2012, Siratovich et al., 2014]). Intact sedimentary rock strength is dependent on a variety of factors  
414 including the rock's diagenetic history, composition, maturity level (well-sorted, well-rounded), and  
415 the cumulative effect of the various geological processes experienced by them since formation such  
416 as metamorphism and deformation. Here we attempt to determine the controls on the strength of  
417 Waipapa greywacke.

418

419 In Waipapa greywacke porosity ranges from 0.841 to 1.304 % (Table 3). These  
420 measurements of low porosity, coupled with the microstructural observations (Figure 3) illustrate  
421 the minimal primary porosity that exists within this lithology. The presence of microcracks in a low  
422 porosity lithology often contribute little to the overall porosity but can have an important impact on  
423 its mechanical strength, and thus the stresses at which it will experience brittle failure [Siratovich et  
424 al., 2014; Eberhardt et al., 1999; Faulkner et al., 2006; Lajtai, 1998]. Previous studies on low  
425 porosity crystalline rocks have shown that the presence of microfractures is evident by deviation  
426 from linear elastic behaviour at stress levels well below the failure stress, as well as an increase in  
427 volumetric strain [Mitchell and Faulkner, 2008; Zoback and Byerlee, 1975]. Both these  
428 observations lend support to the interpretation that, as loading progresses, existing microfractures  
429 start to propagate, leading to reduced compliance (related to deviation from linear elasticity) and  
430 volumetric strain increase.

431

432 There is strong evidence, in addition to the low porosity, that Waipapa greywacke has a low  
433 microcrack density. The loading curve (Figure 4) indicates little dilatancy from the volumetric  
434 strain curve and there is an appreciable lack of any yield point. This indicates that the formation of  
435 any microcrack network prior to failure is very limited, and contrasts with other studies on low



436 porosity rock [Mitchell and Faulkner, 2008; Eberhardt et al., 1999; Zoback and Byerlee, 1975].  
 437 Moreover, the direct dilatancy measurements made via volumetry during the triaxial test also  
 438 indicate little or no dilatancy prior to failure.

439  
 440 Elastic wave velocities can be strongly attenuated by the presence of microcracks in  
 441 crystalline rocks [Siratovich et al., 2014; Vinciguerra et al., 2005; Blake et al., 2012; Heap et al.,  
 442 2014] such that microcracking can strongly reduce  $V_p$  and  $V_s$ . The mechanical test results from the  
 443 Waipapa greywackes show, at the beginning of both the UCS tests and the triaxial loading test,  
 444 there is a short-lived  $V_p$  and  $V_s$  increase, possibly representing closure of some rare microcracks  
 445 present in intact greywacke sample. However, with further loading, changes in  $V_p$  and  $V_s$  are  
 446 minimal and, importantly, show no appreciable decrease immediately before failure that might  
 447 indicate the development of a microcrack network (Figure 4; Figure 8).

448  
 449 The lack of microcracks within intact Waipapa greywacke is interesting given this lithology  
 450 is heavily fractured in-situ. It may be that brittle damage is very localized around macrofractures, as  
 451 we observed in our failed sample from our triaxial deformation experiment here (Figure 7).  
 452 Reloading of the failed sample shows a much shallower gradient than initial (pre-failure) loading,  
 453 indicating that the Young's modulus has appreciably decreased and the fractured sample is much  
 454 more compliant, consistent with the presence of a larger population of microcracks, particularly in  
 455 the near vicinity of the microfracture.

456  
 457

<b>Property</b>	<b>TTGW (this study)</b>	<b># of Tests</b>	<b>WAGW</b>	<b># of Tests</b>	<b>Rotokawa Andesite</b>	<b># of Tests</b>
Tensile Strength (MPa)	14.4 - 32.42	10	20.3 - 35.7	8	9.99 - 24.13	12
UCS (MPa)	205 - 384	10	301 - 310	2	60 - 211	22
Poisson's Ratio ( $\nu$ )	0.19 - 0.54	10	0.28 - 0.29	2	0.09 - 0.34	22

Young's Modulus ( $E$ ) (GPa)	54 - 85	10	65 - 70	2	20 - 44	22
Poisson's Ratio ( $\nu_d$ )	0.28 - 0.30	3	-	-	0.13 - 0.23	22
Young's Modulus ( $E_d$ ) (GPa)	80 - 84	3	-	-	25 - 46	22
Density ( $\rho$ ) (g/cm <sup>3</sup> )	2.727	3	2.71	2	2.49	22
Porosity ( $\phi$ ) (vol%)	1.035	17	~ 2	2	8.44	22

458

459 **Table 3:** A comparison of the physical and elastic properties values for Waipapa greywacke samples (TTGW =  
460 Taotaorao Quarry; WAGW = Waotu Quarry) measured in this study [this study; McNamara et al., 2014] and Torlesse  
461 greywacke [this study (porosity); McNamara et al., 2014, Stewart, 2007], Rototawa andesite [Siratovich et al., 2012,  
462 Siratovich et al., 2014]. Mean values are reported for density and porosity. Dynamic properties are identified in this  
463 table with the subscript "d" ( $E_d$  and  $\nu_d$ ).

464

## 465 **4.2 Waipapa greywacke permeability**

466 The arguments presented above for the low microfracture density of the Waipapa greywacke  
467 have significant implications for the matrix permeability of this rock. The microcrack density does  
468 not have a great influence on the porosity, but the permeability is strongly affected by the presence  
469 of microcracks [Costa, 2006; Chaki, 2008], though this is strongly dependent on effective stress  
470 levels and whether the rock undergoes brittle failure or not [Faulkner and Armitage, 2013; Zoback  
471 and Byerlee, 1975]. In this study, Waipapa greywacke displayed no sign of significant dilatancy  
472 during deformation experiments (Figs. 4-6), and a lack of decrease in  $V_p$  and  $V_s$  before failure in  
473 both uniaxial and triaxial tests. This is complemented by the absence of enhanced permeability  
474 observed during loading to failure in the triaxial deformation experiment (Figure 5). In terms of  
475 macrofracture generation within intact Waipapa greywacke, it appears that dilation of axially  
476 aligned microcracks and their subsequent coalescence plays a limited role in the brittle deformation  
477 and permeability development of this lithology, occurring at stress levels commensurate with those  
478 at failure.

479           The results given in Table 2 are comparable to previous measurements on porosity of  
480 Waipapa greywacke [Mielke et al., 2016], and porosity and permeability measurements made under  
481 the same conditions for Torlesse greywacke ( $\sim 1.6\%$ ,  $\sim 4.824 \times 10^{-22} \text{ m}^2$ ; [McNamara et al., 2014]),  
482 which also hosts geothermal reservoirs [Milicich et al., 2016]. These greywacke lithologies display  
483 the lowest porosity and permeability values measured to date across a range of New Zealand  
484 geothermal lithologies. For comparison, Rotokawa andesite has permeability values four to five  
485 orders of magnitude greater than the greywacke units ( $\sim 10^{-17} \text{ m}^2$ ) [Siratovich et al., 2014], and  
486 greater porosity values (Table 3), while lithologies from the Tahorakuri Formation, Matahina  
487 ignimbrite, Te Teko Formation, Tahuna Formation, and a range of TVZ andesite, dacite, and  
488 rhyolite lavas all have higher average porosity values [Mielke et al., 2016, Wyering et al., 2014].

489           As discussed, inherent microcrack density, porosity, and permeability are linked such that  
490 increased microcrack density, increases porosity, which in turn can increase permeability [Costa,  
491 2006; Chaki et al., 2008], though this is strongly dependant on effective stress levels (Figure 5) and  
492 whether the rock undergoes brittle failure or not [Zoback and Byerlee, 1975]. The low porosity  
493 range reported here for Waipapa greywacke suggests a low density of inherent microstructures in  
494 this lithology, and those that are present are minimally connected. This is supported by the low  
495 permeability measurements ( $1.65 \times 10^{-21} \text{ m}^2$ ), the low reduction in volume observed under triaxial  
496 deformation experiments, and SEM images reported in this study.

497           It has been well demonstrated that faults and fractures in brittle rock are produced by the  
498 interaction and fusion of many microcracks [Mitchell and Faulkner, 2008; Lockner et al., 1991;  
499 Lockner et al., 1992b; Reches and Lockner, 1994; Healy et al., 2006]. As a result, when differential  
500 stress is applied to an intact rock sample, microfracture damage increases as the rock approaches  
501 failure, and the resultant increasing dilatancy will have direct impacts on both porosity and  
502 permeability. For example, permeability increases in Westerly Granite as it is triaxially deformed  
503 are recorded as the granite failure strength is approached due to increasing development of  
504 microcracks, which then increases further as stress is relaxed allowing more connectivity between

505 variable oriented microcracks in the rock [Mitchell and Faulkner, 2008; Zoback and Byerlee, 1975].  
506 In this study, Waipapa greywacke displayed no sign of significant dilatancy during deformation  
507 experiments, both uniaxial and triaxial (Figs. 4-6), similar to results reported in McNamara et al.,  
508 (2014). This lack of dilatancy is supported by the lack of decrease in  $V_p$  and  $V_s$  before failure in both  
509 uniaxial and triaxial tests, and a lack of increased permeability observed during loading in the  
510 triaxial deformation experiment (Figure 5). In terms of macrofracture generation within intact  
511 Waipapa greywacke, it appears that dilation of axially aligned microcracks and their subsequent  
512 coalescence plays either no role in brittle deformation of this lithology, or that it happens within a  
513 fast timeframe not captured by our experimental work here. Concerning contributions pre-failure  
514 deformation makes to Waipapa greywacke permeability, we conclude this is likely to be small,  
515 though suggest future experiments of this nature be performed at higher resolution along the stress-  
516 strain path. Our results suggest that Waipapa permeability is dominated by macrostructures, as no  
517 permeability is witnessed to be generated by dilatancy effects from deformation in this lithology,  
518 agreeing with similar conclusions made elsewhere [McNamara et al., 2014].

519 Passelègue et al. (2018) demonstrate that permeability anisotropy is caused when the intact  
520 rock is loaded to macroscopic failure though the rock being deformed is essentially isotropic,  
521 indicating that permeability anisotropy begins to evolve only after a lithology is deformed, and that  
522 anisotropy will be aligned with respect to the stress state that generated the fractures. Considering  
523 the low permeability of intact Waipapa greywacke, permeability anisotropy is expected to be an  
524 important aspect of this lithology as a geothermal reservoir. Experimental data presented here  
525 confirms the introduction of permeability anisotropy within Waipapa greywacke. Rapid, large  
526 increases in permeability (around four orders of magnitude, from  $10^{-21} \text{ m}^2$  to  $10^{-17} \text{ m}^2$ ) at the point of  
527 brittle failure are noted from the triaxial compression experiment (Figure 5) and the single fracture  
528 permeability tests (Figure 10). Thus, permeability dramatically increases in Waipapa greywacke  
529 rocks as a result of brittle deformation, implying an anisotropic permeability will develop, oriented  
530 with respect to a given stress field.

531 Defining the orientation of such permeable anisotropy in Waipapa greywacke not simple  
532 given the complex nature of the tectonics associated with this lithology in geothermal regions  
533 [McNamara et al., 2019]. Within the TVZ the Waipapa greywacke is subject to NW-SE directed  
534 extension, with local variations [McNamara et al., 2019]. Under contemporary tectonic conditions,  
535 fractures generated in Waipapa greywacke will predominantly align to this stress state (striking NE-  
536 SW, parallel to  $\sigma_2$ ), thus defining the permeability anisotropy. However, the Waipapa greywacke  
537 has undergone deformation prior to TVZ rifting resulting in previous brittle deformation in a range  
538 of orientations [Roland and Sibson, 2004]. We suggest that lateral permeability anisotropy in  
539 Waipapa greywacke will be aligned to the strike of the TVZ rift (NE-SW), in which both brittle  
540 structures formed during rifting, and brittle structures formed pre-rifting, but preferentially aligned  
541 for slip in the current stress field, control geothermal fluid flow. Indeed, a dominant NE-SW  
542 fracture strike orientation is shown within fluid flow zones in geothermal wells drilled into Torlesse  
543 greywacke basement at the Kawerau Geothermal Field [Wallis et al., 2004], establishing these  
544 fracture patterns do exist in greywacke basement type lithologies in the TVZ. Implications of our  
545 findings for geothermal fluid flow in the Waipapa greywacke reservoir Ngawha Geothermal Field  
546 are more difficult to determine due to a lack of direct structural or stress information from this  
547 location [Mongillo, 1985]. Reported structures have E-W, and NE-SW strike orientations and are  
548 associated with NW-SE directed extension in the region [Bayrante and Spörli, 1989]. Assuming this  
549 structure-stress arrangement, we can infer from our experimental results that a macrofracture related  
550 permeability anisotropy aligned NE-SW would form in the Waipapa basement of the Ngawha  
551 Geothermal Field.

552 In a geothermal reservoir where permeability is controlled by macrostructures, such as those  
553 in Waipapa greywacke, the ability for brittle structures to maintain fluid flow is important to the  
554 resource longevity and sustainability. This study examined the effect of single macrofracture  
555 behavior on the permeability of Waipapa greywacke. Macrofracture closure pressures of  
556 synthetically generated fractures in Waipapa greywacke falls between 95 to 112 MPa. At these

557 closure pressures, fluid flow across the fracture was observed to continue, developing a stable  
558 permeability around  $10^{-19}$  m<sup>2</sup> for confining pressures between 95 and 150 MPa (Figure 10). Thus,  
559 even at closure, macrofractures in the Waipapa greywacke provide continued permeability (2 orders  
560 of magnitude higher than intact greywacke permeability). Permeability measurements on fractured  
561 greywacke under triaxial conditions also support persistent permeability in greywacke fractures post  
562 initial failure (Figure 5). Similar large increases in permeability from inducing a single fracture are  
563 reported from dense volcanic rocks in geothermal regions [Lamur et al., 2017]. Persistent  
564 permeability in Waipapa greywacke fractures under closure pressures may be facilitated by  
565 incomplete fracture closure due to the presence of fragments inside the fractures propping it open,  
566 asperity generation, permeability via secondary brittle damage generated around the main brittle  
567 fracture (Figure 10). Our observations suggest all three possibilities may contribute in some way. A  
568 size range of wall rock fragments are observed within the triaxial fracture experiment, some of  
569 which are likely more than significant to prop open a newly generated fractures and facilitate  
570 ongoing fluid flow within it. The longevity of this propping is uncertain, as over time with ongoing  
571 fracture slip, these fragments may be constantly reduced in size and maintain less open space. With  
572 enough time and comminution of fracture fill material, combined with fluid-rock interaction, gouge  
573 may be generated and potentially seal the fracture completely to fluid flow. Asperity generation in  
574 fractures tested here will certainly play a role in ongoing fracture permeability after closure  
575 pressures are reached, as morphologically different fracture walls are observed in fractures  
576 generated in both triaxial and tensile tests. As with grain propping, there is a time limit to the ability  
577 for asperity to maintain fluid flow in a fracture as consistent slip will eventually grind these  
578 asperities down. The exact contribution secondary brittle damage makes to observed greywacke  
579 permeability is unknown, which makes it difficult to address in terms of their contribution to  
580 permeability under closure pressures. Given these secondary structures generated under the same  
581 experimental conditions as the primary brittle failure it is reasonable to assume they would behave

582 similarly to the main fracture, though given their more varied orientation with respect to  $\sigma_1$ , and the  
583 high level of intersection observed this is questionable and requires further study.

584

585 It should be noted that the results from the measurements on the single fracture are  
586 represented in terms of permeability to allow direct comparison with the permeability of the intact  
587 rock. Strictly, reporting permeability for fracture flow is not correct, as the calculation assumes that  
588 fluid flow occurs over the cross-sectional area of the specimen, whereas for rocks with a low matrix  
589 permeability, fluid will predominantly flow through the fracture. Consequently, the 'permeability'  
590 becomes scale dependent [Heap and Kennedy, 2016]. This can be illustrated by considering that if  
591 the sample diameter were doubled, the flow would also double, as the length of the fracture has  
592 increased by a factor of two. However, the cross-sectional area used in the permeability calculation  
593 would quadruple and the permeability would appear to half for the larger specimen. Hydraulic  
594 transmissivity, the product of the fracture permeability and its thickness, is a better way to represent  
595 the flow properties of fractures. This parameter can be derived from the pulse transient  
596 measurements we made using the methodology described by Rutter and Mecklenburgh (2018).

597 In summary, intrinsic microfracture density in Waipapa greywacke is low, and the  
598 development, coalescence, and growth of the microfracture network before failure is minimal.  
599 Consequently, microfractures do not play a key role in the formation of permeable structures within  
600 the Waipapa greywacke lithology. Macrofractures demonstrably increase permeability in Waipapa  
601 greywacke, contribute to long-lived permeability post-failure, and the permeability they develop  
602 within this lithology is anisotropic, and so permeability vectors in the greywacke units will be  
603 related to the local and regional stress conditions.

604

605

606

607

608 **5 CONCLUSIONS**

609 Our experiments indicate a high mechanical strength for intact Waipapa greywacke  
610 lithology that is partly due to a low density of inherent microcracks. This lack of microcracks  
611 contributes to the low intrinsic porosity and permeability of intact Waipapa greywacke. Our  
612 experiments confirm that the Waipapa greywacke lithology will only support fluid flow via the  
613 generation of macrostructures. Furthermore, these macrofractures maintain a level of permeability  
614 after stress conditions relax (fracture closure). Brittle fractures generated in Waipapa greywacke  
615 thus remain important permeable components in this lithology for an undetermined length of time  
616 after their formation. Such macrofracture controlled permeability is inherently anisotropic and as  
617 such the directionality of fluid transmission in the Waipapa greywacke will be strongly controlled  
618 by the arrangement of the local tectonic stress field as this controls orientation of microfracture  
619 development. Given that structures impart strong permeability anisotropy to Waipapa basement,  
620 any fluid flow modeling of geothermal systems within such geological units should account for this.  
621 Further studies on Waipapa greywacke mechanical strength that simulate deeper crustal levels, and  
622 flow experiments through single macrostructures under such conditions are required to better  
623 quantify the fluid flow properties of this basement lithology needed for accurate modelling.

624

625

626

627

628

629

630

631

632

633

**REFERENCES**



634

635 Adams CJ, Mortimer N, Campbell HJ, Griffin WL. Age and isotropic characterisation of  
636 metasedimentary rocks from the Torlesse Supergroup and Waipapa Group in the central  
637 North Island, New Zealand. *New Zealand Journal of Geology and Geophysics*.  
638 2009;52:149-170. <https://doi.org/10.1080/00288300909509883>

639

640 Bayrante LF, Spörli KB. Structural observations in the autochthon and allochthon at Ngawha  
641 geothermal field, New Zealand. *Geology of Northland: Accretion, allochthon and arcs at the*  
642 *edge of the New Zealand micro-continent*. Royal Society of New Zealand Bulletin.  
643 1989;26:106-114.

644

645 Beetham RD, Watters WA. Geology of Torlesse and Waipapa terrane basement rocks encountered  
646 during the Tongariro power development project, North Island, New Zealand. *New Zealand*  
647 *journal of geology and geophysics*. 1985;28:575-594.  
648 <https://doi.org/10.1080/00288306.1985.10422534>

649

650 Begg JG, Mazengarb C. Part Q27, scale 1:50,000, Lower Hutt: Institute of Geological & Nuclear  
651 Sciences. Institute of Geological & Nuclear Sciences geological map 22. 128 p. + 1 fold.  
652 Map. 1996.

653

654 Bibby H, Caldwell T, Davey F, Webb T. Geophysical evidence on the structure of the Taupo  
655 Volcanic Zone and its hydrothermal circulation. *Journal of Volcanology and Geothermal*  
656 *Research*. 1995;68:29-58. [https://doi.org/10.1016/0377-0273\(95\)00007-H](https://doi.org/10.1016/0377-0273(95)00007-H)

657

658 Bignall G. Taupo Volcanic Zone deep geothermal drilling project. *Proceedings Hotter and Deeper*  
659 *Exploration Science Workshop, Taupo, New Zealand*. 2011.  
660 <https://www.geothermal-energy.org/pdf/IGAstandard/NZGW/2011/K2.pdf> (2011).  
661 Accessed 31 October 2021.

662

663 Bignall G, Rae A, Rosenberg M. Rationale for targeting fault versus formation-hosted permeability  
664 in high-temperature geothermal systems of the Taupo Volcanic Zone, New Zealand.  
665 *Proceedings, World Geothermal Congress, Bali, Indonesia*. 2010.  
666 <https://www.geothermal-energy.org/pdf/IGAstandard/WGC/2010/1148.pdf> (2010).  
667 Accessed 31 October 2021.

668  
669  
670  
671  
672  
673  
674  
675  
676  
677  
678  
679  
680  
681  
682  
683  
684  
685  
686  
687  
688  
689  
690  
691  
692  
693  
694  
695  
696  
697  
698  
699  
700  
701•  
702

Blake OO, Faulkner DR, Rietbrock A. The effect of varying damage history in crystalline rocks on the P and S wave velocity under hydrostatic confining pressure. *Pure Applied Geophysics*. 2012;170:493-505. <https://doi.org/10.1617/s11527-016-0892-7>

Brace WF, Walsh JB, Frangos WT. Permeability of granite under high pressure. *Journal of Geophysical Research*. 1968;73:2225-2236. <https://doi.org/10.1029/JB073i006p02225>

Brathwaite RL, Wood CP, Rosenberg MD, Faure K. Porosity and permeability in the basement rocks at the Kawerau and Ohaaki geothermal fields, New Zealand. IN: Soengkono S, Browne PRL. *Proceedings, 24th New Zealand Geothermal Workshop, University of Auckland*. 2002;24:49-54. <https://www.geothermal-energy.org/pdf/IGAstandard/NZGW/2002/Brathwaite.pdf> (2002). Accessed 31 October 2021.

Browne PRL. Joint channels in reservoir rocks of the Ngawha geothermal field, Northland. *Proceeding, 2nd New Zealand Geothermal Workshop, University of Auckland*. 1980;81-84. <https://www.geothermal-energy.org/pdf/IGAstandard/NZGW/1980/Browne.pdf> (1980). Accessed 31 October 2021.

Cant JL, Siratovich PA, Cole JW, Villeneuve MC, Kennedy BM. Matrix permeability of reservoir rocks, Ngatamariki geothermal field, Taupo Volcanic Zone, New Zealand. *Geothermal Energy*. 2018;6. <http://dx.doi.org/10.26021/8877>

Carey B, Dunstall M, McClintock S, White B, Bignall G, Luketina K, Robson B, Zarrouk S, Seyward A. *New Zealand country update*. World Geothermal Congress, Melbourne. 2015.

Chaki S, Takarli M, Agbodjan WP. Influence of thermal damage on physical properties of a granite rock: porosity, permeability and ultrasonic wave evolutions. *Construction and Building Materials*. 2008;22:1456-1461. <https://doi.org/10.1016/j.conbuildmat.2007.04.002>

Cole JW, Spinks KD. *Caldera volcanism and rift structure in the Taupo Volcanic Zone, New Zealand*. Geological Society, London, Special Publications. 2009;327:9-29. <http://dx.doi.org/10.1144/SP327.2>

703 Costa A. Permeability-porosity relationship: A reexamination of the Kozeny-Carman equation  
704 based on a fractal pore-space geometry assumption. *Geophysical research letters*. 2006.  
705 <https://doi.org/10.1029/2005GL025134>  
706

707 Cox ME, Browne PRL. Hydrothermal alteration mineralogy as an indicator of hydrology at the  
708 Ngawha Geothermal Field, New Zealand. *Geothermics*. 1998;27:259-270.  
709 [https://doi.org/10.1016/S0375-6505\(97\)10015-3](https://doi.org/10.1016/S0375-6505(97)10015-3)  
710

711 Di Pippo R. *Geothermal power plants: principles, applications, case studies and environmental*  
712 *impact*. Elsevier Ltd, 2nd edition, Oxford. 2008.  
713

714 Eberhardt E, Stead D, Stimpson B. Quantifying progressive pre-peak brittle fracture damage in rock  
715 during uniaxial compression. *International Journal of Rock Mechanics and Mining Sciences*.  
716 1999;36:361-380. [https://doi.org/10.1016/S0148-9062\(99\)00019-4](https://doi.org/10.1016/S0148-9062(99)00019-4)  
717

718 Evans KF, Genter A, Sausse J. Permeability creation and damage due to massive fluid injections  
719 into granite at 3.5 km at Soultz: 1. Borehole observations. *Journal of Geophysical Research*  
720 *e Solid Earth*. 2005;110(B4). <https://doi.org/10.1029/2004JB003168>  
721

722 Faulkner DR, Armitage PJ. The effect of tectonic environment on permeability development around  
723 faults and in the brittle crust. *Earth and Planetary Science Letters*. 2013;375:71-77.  
724 <https://doi.org/10.1016/j.epsl.2013.05.006>  
725

726 Faulkner DR, Mitchell TM, Healy D, Heap MJ. Slip on "weak" faults by the rotation of regional  
727 stress in the fracture damage zone. *Nature*. 2006;444:922-925.  
728 <https://doi.org/10.1038/nature05353>  
729

730 Gale JFW, Holder J. Natural fractures in the Barnett Shale: Constraints on spatial organization and  
731 tensile strength with implications for hydraulic fracture treatment in Shale-Gas reservoirs.  
732 In: 42nd U.S. Rock Mechanics Symposium & 2nd U.S.-Canada Rock Mechanics  
733 Symposium: ARMA. 2008;08-96.  
734

735 Grant MA, Bixley PF. *Geothermal Reservoir Engineering*, 2nd edition, Academic Press,  
736 Burlington, USA. 2011. doi:[10.1016/C2010-0-64792-4](https://doi.org/10.1016/C2010-0-64792-4)

737

738 Gupta H, Sukanta R. An alternative resource for the 21st Century. Geothermal Energy, 1st edition,  
739 Elsevier Science. 2006.

740

741 Healy D, Jones RR, Holdsworth RE. Three-dimensional brittle shear fracturing by tensile crack  
742 interaction. Nature. 2006;439:64-67. <https://doi.org/10.1038/nature04346>

743

744 Heap MJ, Faulkner DR. Quantifying the evolution of static elastic properties as crystalline rock  
745 approaches failure. International Journal of Rock Mechanics and Mining Sciences.  
746 2008;45:564-573.

747

748 Heap MJ, Kennedy B. Exploring the scale-dependent permeability of fractured andesite. Earth and  
749 Planetary Science Letters. 2016;447:139-150. <https://doi.org/10.1016/j.epsl.2016.05.004>

750

751 Heap MJ, Lavallée Y, Petrakova L, Baud P, Reuschlé T, Varley NR, Dingwell DB. Microstructural  
752 controls on the physical and mechanical properties of edifice-forming andesites at Volcán de  
753 Colima, Mexico. Journal of Geophysical Research, Solid Earth. 2014;119:2925-2963.  
754 <https://doi.org/10.1002/2013JB010521>

755

756 Kuttruff H. Ultrasonics fundamentals and applications. Elsevier, Science & Technology, New York.  
757 1991.

758

759 Lajtai EZ. Microscopic fracture processes in a granite. Rock Mechanics and Rock Engineering.  
760 1998;31:237-250. <https://doi.org/10.1007/s006030050023>

761

762 Lamur A, Kendrick JE, Eggertsson GH, Wall RJ, Ashworth JD, Lavallée Y. The permeability of  
763 fractured rocks in pressurised volcanic and geothermal systems. Scientific reports.  
764 2017;7:61-73. <https://doi.org/10.1038/s41598-017-05460-4>

765

766

767 Lockner DA, Byerlee JD, Kuksenko V, Ponomarev A, Sidorin A. Quasi-static fault growth and  
768 shear fracture energy in granite, Nature. 1991;350:39-42. <https://doi.org/10.1038/350039a0>

769

770 Lockner DA, Byerlee JD, Kuksenko V, Ponomarev A, A, Sidrin. Observations of quasi-static fault  
771 growth from acoustic emissions, *Fault Mechanics and Transport Properties of Rocks*, edited  
772 by Evans B, and Wong TF. Academic, San Diego, California. 1992b:3-31.  
773

774 Mayer W. Petrology of the Waipapa Group, near Auckland, New Zealand. *New Zealand Journal of*  
775 *Geology and Geophysics*. 1968;12:412-435.  
776 <https://doi.org/10.1080/00288306.1969.10420291>  
777

778 McGuinness MJ. Recent interference tests at Ngawha and Ohaaki. *Proceedings, 6th New Zealand*  
779 *Geothermal Workshop*. 1984;169-174.  
780 <https://pangea.stanford.edu/ERE/pdf/IGAstandard/NZGW/1984/McGuinness.pdf> (1984).  
781

782 McNamara DD, Faulkner DR, McCarney E. Rock Properties of Greywacke Basement Hosting  
783 Geothermal Reservoirs, New Zealand, preliminary results. *Proceedings, 39th Workshop*  
784 *Geothermal Reservoir Engineering*, Stanford University, California. 2014;10-21.  
785 doi:10.13140/RG.2.1.1304.2160  
786

787 McNamara DD, Massiot C. Geothermal structural geology in New Zealand: Innovative  
788 Characterisation and micro-analytical techniques. *Proceedings, 38th New Zealand*  
789 *Geothermal Workshop*, Auckland, New Zealand. 2016.  
790 [https://www.geothermal-energy.org/pdf/IGAstandard/NZGW/2016/Keynote\\_McNamara.pdf](https://www.geothermal-energy.org/pdf/IGAstandard/NZGW/2016/Keynote_McNamara.pdf)  
791 (2016). Accessed 31 October 2021.  
792

793 McNamara DD, Milicich SD, Massiot C, Villamor P, McLean K, Sépulveda F, Ries WF. Tectonic  
794 controls on Taupo Volcanic Zone geothermal expression: Insights from Te Mihi, Wairakei  
795 Geothermal Field. *Tectonics*. 2019. <https://doi.org/10.1029/2018TC005296>  
796

797 McNamara DD, Sewell S, Buscarlet E, Wallis IC. A review of the Rotokawa Geothermal Field,  
798 New Zealand. *Geothermics*. 2016;59:281-293.  
799 <https://doi.org/10.1016/j.geothermics.2015.07.007>  
800

801 Mielke P, Weinert S, Bignall G, Sass I. Thermo-physical rock properties of greywacke basement  
802 rock and intrusive lavas from the Taupo Volcanic Zone, New Zealand. *Journal of*  
803 *Volcanology and Geothermal Research*. 2016;324:179-189.

804 <https://doi.org/10.1016/j.jvolgeores.2016.06.002>  
805  
806 Milicich SD, Clark JP, Wong C, Askari M. A review of the Kawerau geothermal field. New  
807 Zealand. *Geothermics*. 2016;59:252-265. <https://doi.org/10.1016/j.jvolgeores.2018.01.012>  
808  
809 Milicich SD, Wilson CJN, Bignall G, Pezaro B, Charlier BLA, Wooden JL, Ireland TR. U–Pb  
810 dating of zircon in hydrothermally altered rocks of the Kawerau Geothermal Field, Taupo  
811 Volcanic Zone, New Zealand. *Journal of Volcanology and Geothermal Research*.  
812 2013a;253:97-113. <https://doi.org/10.1016/j.jvolgeores.2012.12.016>  
813  
814 Mitchell TM, Faulkner DR. Experimental measurements of permeability evolution during triaxial  
815 compression of initially intact crystalline rocks and implications for fluid flow in fault  
816 zones. *Journal of Geophysical Research*. 2008;113. <https://doi.org/10.1029/2008JB005588>  
817  
818 Mongillo MA. The Ngawha geothermal field: new and updated scientific investigations.  
819 Geothermal Coordination Group, Department of Scientific and Industrial Research. 1985.  
820  
821 Mroczek EK, Milicich SD, Bixley PF, Sepulveda F, Bertrand EA, Soengkono S, Rae AJ. Ohaaki  
822 geothermal system: Refinement of a conceptual reservoir model. *Geothermics*. 2016;59:311-  
823 324. <https://doi.org/10.1016/j.geothermics.2015.09.002>  
824  
825 Nara Y, Meredith PG, Yoneda T, Kaneko K. Influence of macro-fractures and micro-fractures on  
826 permeability and elastic wave velocities in basalt at elevated pressure. *Tectonophysics*.  
827 2011;503:52-59. <https://doi.org/10.1016/j.tecto.2010.09.027>  
828  
829 Passelègue FX, Pimienta L, Faulkner DR, Schubnel A, Fortin JN, Guéguen Y. Development and  
830 recovery of stress-induced elastic anisotropy during cyclic loading experiment on Westerley  
831 granite. *Geophysical Research Letters*. 2018;45:8156-816.  
832 <https://doi.org/10.1029/2018GL078434>  
833  
834 Paterson M, Wong T. *Experimental rock deformation - The brittle field*. Springer-Verlag. 2005;12-  
835 13.  
836

837 Reches Z, Lockner DA. Nucleation and growth of faults in brittle rocks. *Journal of Geophysics*  
838 *Research*. 1994;99:159-173. <https://doi.org/10.1029/94JB00115>  
839

840 Richards L, Read S. New Zealand greywacke characteristics and influences on rock mass behavior.  
841 *Proceedings, 11th Congress of the International Society of Rock Mechanics: the second half*  
842 *century of rock mechanics*. 2007;359-364.  
843

844 Rowland JV, Sibson RH. Structural controls on hydrothermal flow in a segmented rift system,  
845 *Taupo Volcanic Zone, New Zealand*. *Geofluids*. 2004;4:259-283.  
846 <https://doi.org/10.1111/j.1468-8123.2004.00091.x>  
847

848 Rutter EH, Mecklenburgh J. Influence of normal and shear stress on the hydraulic transmissivity of  
849 thin cracks in a tight quartz sandstone, a granite, and a shale. *Geophysical Research: Solid*  
850 *Earth*. 2018;123. <https://doi.org/10.1002/2017JB014858>  
851

852 Sheppard DS. Fluid chemistry of the Waimangu geothermal system. *Geothermics*. 1986;15:309-  
853 328. [https://doi.org/10.1016/0375-6505\(86\)90107-0](https://doi.org/10.1016/0375-6505(86)90107-0)  
854

855 Sherburn S, Bannister SC, Bibby HM. Seismic velocity structure of the central Taupo Volcanic  
856 *Zone, New Zealand, from local earthquake tomography*. *Journal of Volcanology and*  
857 *Geothermal Research*. 2003;122:69-88. [https://doi.org/10.1016/S0377-0273\(02\)00470-5](https://doi.org/10.1016/S0377-0273(02)00470-5)  
858

859 Siratovich PA, Davidson J, Villeneuve M, Graveley D, Kennedy B, Cole J, Wyering L, Price L.  
860 *Physical and mechanical properties of the Rotokawa Andesite from production wells RK*  
861 *27\_L2, RK 28 and RK 30*. *Proceedings, New Zealand Geothermal Workshop, University of*  
862 *Auckland, New Zealand*. 2012.  
863 <https://www.geothermal-energy.org/pdf/IGAstandard/NZGW/2012/46654final00022.pdf>  
864

865 Siratovich PA, Heap MJ, Villeneuve MC, Cole JW, Reuschlé T. Physical property relationships of  
866 the Rotokawa Andesite, a significant geothermal reservoir rock in the Taupo Volcanic Zone,  
867 *New Zealand*. *Geothermal Energy*. 2014;2:1-31.  
868 <https://doi.org/10.1186/s40517-014-0010-4>  
869

870 Siratovich PA, Von Aulock FW, Lavallée Y, Cole JW, Kennedy BM, Villeneuve MC.  
871 Thermoelastic properties of the Rotokawa Andesite: A geothermal reservoir constraint.  
872 Journal of Volcanology and Geothermal Research. 2015;301:1-13.  
873 <http://dx.doi.org/10.1016/j.jvolgeores.2015.05.003>.  
874

875 Stewart S. Rock mass strength and deformability of unweathered closely jointed New Zealand  
876 greywacke, PhD Thesis, University of Canterbury, Christchurch, New Zealand. 2007.  
877 <http://dx.doi.org/10.26021/3499>  
878

879 Sutherland R, Townend J, Toy V, Zimmer M. Extreme hydrothermal conditions at an active plate-  
880 bounding fault. Nature. 2017;546:137-140. <https://doi.org/10.1038/nature22355>  
881

882 Vinciguerra S, Trovato C, Meredith PG, Benson PM. Relating seismic velocities, thermal cracking  
883 and permeability in Mt. Etna and Iceland basalts. International Journal of Rock Mechanics  
884 and Mining Sciences. 2005;42:900-910. <https://doi.org/10.1016/j.ijrmms.2005.05.022>  
885

886 Wallis IC, Bardsley CJ, Powell TS, Rowland JV, O'Brien JM. A structural model for the Rotokawa  
887 Geothermal Field, New Zealand. Proceedings, 35th New Zealand Geothermal Workshop,  
888 Auckland University, New Zealand. 2013.  
889

890 Wallis I, McNamara DD, Rowland J, Massiot C. The nature of fracture permeability in the  
891 greywacke basement at Kawerau Geothermal Field, New Zealand. In Proceedings, 37th  
892 Workshop on Geothermal Reservoir Engineering. 2012. doi:10.13140/RG.2.1.4875.9284  
893

894 Wilson CJN, Houghton BF, McWilliams MO, Lanphere MA, Weaver SD, Briggs RM. Volcanic  
895 and structural evolution of Taupo Volcanic Zone, New Zealand, a review. Journal of  
896 Volcanology and Geothermal Research. 1995;68:1-28.  
897

898 Wood C, Brathwaite RL, Rosenberg MD. Basement structure, lithology and permeability at  
899 Kawerau and Ohaaki geothermal fields, New Zealand. Geothermics. 2001;30:461-481.  
900 [https://doi.org/10.1016/S0375-6505\(01\)00003-7](https://doi.org/10.1016/S0375-6505(01)00003-7)  
901



902 Wyering LD, Villeneuve MC, Walli, IC, Siratovich PA, Kennedy BM, Gravley DM, Cant JL.  
903 Mechanical and physical properties of hydrothermally altered rocks, Taupo Volcanic Zone,  
904 New Zealand. 2014. <https://doi.org/10.1016/j.jvolgeores.2014.10.008>

905

906 Zoback MD, Byerlee JD. The effect of microcrack dilatancy on the permeability of Westerly  
907 granite. Journal of Geophysical Research. 1975;80:752-755.

908 <https://doi.org/10.1029/JB080i005p00752>

909

910

911

912

913

## Declarations

914

915

916

## Availability of data and materials

917

918

919 The datasets used and analyzed during the current study are available and have been attached as  
920 submitting files. Information and settings about the machines employed in the experiments are  
921 available at Rock Deformation Laboratory - Department of Earth, Ocean and Ecological Sciences -  
922 University of Liverpool (UK).

923

924

925

926

## Competing Interests

927

928

929 The authors declare that they have no competing interests regarding the publication of this article.

930

931

932

933

## Funding Statement

934

935 This research was supported and funded by the New Zealand Ministry of Business, Innovation and  
936 Employment Geothermal Supermodels research programme hosted by GNS Science.

937

938

939

## Author's contributions

940

941 AM planned study strategy, made the rock samples for the tests, designed the jig for Brazilian test,  
942 performed all scientific experiments and measurements, analyzed and interpreted the experiments'  
943 data, observed thin sections at optical and SEM microscopes, built up graphs for the data  
944 interpretations, designed a schematic illustration of the sample assembly, made all the data tables  
945 presenting data collections, contributed in writing the manuscript.

946

947 DRF planned study strategy, supervised laboratory operations, analyzed and interpreted the  
948 experiments' data, contributed in writing the manuscript.

949

950 DDM planned study strategy, provided rough rock samples from the field, collected SEM images,  
951 analyzed and interpreted the experiments' data, contributed in writing the manuscript.

952

953 All authors read and approved the final manuscript.

954

955

956

957

## Acknowledgements

958

959 We thank Julian Mecklenburgh for discussions of research results. We acknowledge the research  
960 staff and technicians of the University of Liverpool's Rock Deformation Laboratory (Gary  
961 Coughlan) and Scanning Electron Microscopy Shared Research Facility (Elliot Wood) for access to,  
962 use of, and training on equipment and microscopes.

963

964

965

966

967

968

## Supplementary Files

This is a list of supplementary files associated with this preprint. Click to download.

- [Data.rar](#)